NdBaFe$_2$O$_{5+w}$ and steric effect of Nd on valence mixing and ordering of Fe

J. Lindén [a], P. Karen [b],*

[a] *Department of Physics, Åbo Akademi, FI-20500 Turku, Finland*
[b] *Department of Chemistry, University of Oslo, P.O.Box 1033, Blindern, N-0315 Oslo, Norway*

ABSTRACT

NdBaFe$_2$O$_5$ above and below Verwey transition is studied by synchrotron X-ray powder diffraction and Mössbauer spectroscopy and compared with GdBaFe$_2$O$_5$ that adopts a higher-symmetry charge-ordered structure typical of the Sm–Ho variants of the title phase. Differences are investigated by Mössbauer spectroscopy accounting for iron valence states at their local magnetic and ionic environments. In the charge-ordered state, the orientation of the electric-field gradient (EFG) versus the internal magnetic field (B) agrees with experiment only when contribution from charges of the ordered d_{xz} orbitals of Fe^{2+} is included, proving thus the orbital ordering. The EFG magnitude indicates that only some 60% of the orbital order occurring in the Sm–Ho variants is achieved in NdBaFe$_2$O$_5$. The consequent diminishing of the orbit contribution (of opposite sign) to the field B at the Fe^{2+} nucleus explains why B is larger than for the Sm–Ho variants. The decreased orbital ordering in NdBaFe$_2$O$_5$ causes a corresponding decrease in charge ordering, which is achieved by decreasing both the amount of the charge-ordered iron states in the sample and their fractional valence separation as seen by the Mössbauer isomer shift. The charge ordering in NdBaFe$_2$O$_{5+w}$ is more easily suppressed by the oxygen nonstoichiometry (w) than in the Sm–Ho variants. Also the valence mixing into Fe$^{2.5+}$ is destabilized by the large size of Nd. The orientation of the EFG around this valence-mixed iron can only be accounted for when the valence-mixing electron is included in the electrostatic ligand field. This proves that the valence mixing occurs between the two iron atoms facing each other across the structural plane of the rare-earth atoms.

1. Introduction

Under favorable magnetic order, mixed-valence oxides of the Robin–Day type III [1] are candidate materials for spin-polarized conduction and future spintronics. The thermally induced transition into the Robin–Day type III, valence-mixed, Fe$^{2.5+}$ state is called the Verwey transition. RBaFe$_2$O$_5$ perovskites are good model phases with a strong first-order transition of such type [2–4]. Surprisingly, the transition parameters depend on the rare-earth element R. As an example, the transition temperature T_V decreases from 315 K for R = Ho to 215 K for R = Nd [5]. The transition actually proceeds in two steps in RBaFe$_2$O$_5$ [2]: Upon cooling, the valence-mixed phase first shows an incipient, premonitory, partial separation of charges into a disordered arrangement at T_p. Then about 30 K below T_p, the main Verwey transition occurs into a long-range structural order of Fe^{2+} and Fe^{3+}. Both charge ordering and valence mixing are cooperative phenomena [6]; the former proceeds via packing of the d_{xz} orbitals of Fe^{2+} [7] whereas the latter is a dynamical probabilistic process of mixing Fe^{2+} and Fe^{3+} [8]. It is therefore likely that

sterical interferences of R with valence mixing and charge ordering in these phases are of different kind.

NdBaFe$_2$O$_5$ is different in several aspects from its Sm–Ho cousins. As shown in Ref. [4], when the projected trend in the volume increase upon charge ordering becomes too large, NdBaFe$_2$O$_5$ distorts (*Pmma* to *P* 2$_1$*ma*) to achieve a long-range charge ordering of similar extent as R=Sm, but under volume expansion as small as for R=Dy. The discontinuous changes at the main Verwey transition in volume, orthorhombic distortion, entropy and electrical conductivity are smallest for NdBaFe$_2$O$_5$. They also disappear at lower levels of the oxygen nonstoichiometry (w in RBaFe$_2$O$_{5+w}$) than for the other R variants [3,5].

Questions addressed in this study concern factors that influence stability of the ordered and mixed states: What is behind the lower stability of charge-ordered NdBaFe$_2$O$_5$, a less stable charge ordering, orbital ordering, or a more stable valence mixing? Is charge ordering in NdBaFe$_2$O$_5$ weaker and less robust because it is incomplete or because of lower concentrations of the charge-ordered states? Is the thermally induced valence mixing in NdBaFe$_2$O$_{5+w}$ less robust because the mixing is incomplete, or owing to lower concentration of Fe$^{2.5+}$?

The answers are obtained with ^{57}Fe Mössbauer spectroscopy, which is able to account for all valence and spin states of iron and their local magnetic and ionic environments while taking special

advantage of their distortions that enrich the spectral features. High-resolution synchrotron X-ray powder diffraction (SXPD) is used to obtain structural data for calculations of energies of molecular orbitals of the 3d parentage and of the electric-field gradients experienced by the Mössbauer nucleus. Modeling the Mössbauer spectra is then used to extract the local environments of the charge-ordered and valence-mixed species.

2. Experimental

Syntheses and characterization: A series of single-phase NdBa-Fe_2O_{5+w} samples of varied nonstoichiometry was synthesized from amorphous precursors obtained by liquid mixing in melted citric acid, as described in Ref. [3], followed by isothermal equilibration in a flowing atmosphere of a controlled partial pressure of oxygen [9] and quenching. Synthesis conditions for a typical sample are listed in Table 1. For comparisons between the two charge-ordered structure types, the $GdBaFe_2O_{\sim 5}$ phase was synthesized. A homogeneous oxygen content in $NdBaFe_2O_{5.001}$ and $GdBaFe_2O_{5.009}$ was achieved under a final annealing at 400 °C for 25 days in evacuated silica ampoules gettered by Zr kept at 700 °C, followed by slow cooling at a rate of 0.1 °C/min. The oxygen nonstoichiometry w was determined cerimetrically, after digestion of the samples using a closed-ampoule technique developed earlier [10].

SXPD: Data for $NdBaFe_2O_{5.001}$ and $GdBaFe_2O_{5.009}$ were collected on the high-intensity, high-resolution ID31 diffractometer at the ESRF Grenoble. The powder sample was sealed in a glass capillary of 0.35 mm in diameter and rotated at $60 s^{-1}$ in the beam of wavelength 0.4002 Å. Diffracted intensities were recorded in steps of 0.0005° 2θ over a redundant angular range to ensure good contribution from all nine parallel detectors, and then averaged into steps of 0.0015° 2θ. Data collection at 100 K between −6 and 30° 2θ at the detector 1 took 3 h, between 30 and 45° 2.5 h. The temperature was controlled by nitrogen flow from a 700 series Oxford Cryostream Plus. Short isothermal scans were performed between 2 and 26° across the main Verwey transition and averaged into step size of 0.002° in 2θ. Rietveld refinements were done with the GSAS software suite [11]. Strain anisotropy coefficients [12] S_{hkl} were used to model the asymmetry of Bragg peaks caused by the distribution of the oxygen nonstoichiometry [13] across the sample.

Orbital energy calculations: The molecular-orbital energy levels for iron–oxygen anionic coordinations were estimated from structural data by the extended Hückel tight-binding method as implemented in the CAESAR 2.0 (Crystal And Electronic Structure AnalyzeR) software package [14], with the basis-set coefficients listed previously [7].

Mössbauer spectroscopy: The Mössbauer absorbers were made by spreading ~70 mg of the sample in an epoxy resin across an area of ~3.0 cm^2 on an Al foil. Measurements were performed using Cyclotron Co. sources $^{57}Co:Rh$ (25 mCi, January 2002 and 25 mCi, January 2004) at fixed temperatures between 77 and 300 K, in transmission geometry with a maximum Doppler

velocity of 11.15 mm/s. An additional measurement at 448 K was also done for the stoichiometric $NdBaFe_2O_{5.001}$ sample using a Doppler velocity of 2.0 mm/s.

All spectra recorded below the Néel temperature exhibited cooperative magnetic splitting and were fitted with the full Hamiltonian of combined electric and magnetic interactions using the following parameters: the internal magnetic field experienced by the Fe nucleus (B) and its Gaussian distribution of the width ΔB, the chemical isomer shift relative to α−Fe (δ), the relative intensities of the components (I), the resonance line widths (Γ), constrained to be equal for all spectral components, and, finally, the parameters of the electric interaction. The electric hyperfine interaction is based on the electric-field gradient (EFG) acting on the Fe nucleus. EFG is a 2nd rank tensor, usually denoted as a matrix V_{ij}, $i, j = 1, 2, 3$. The matrix can be diagonalized, and, in the end, only two terms are necessary: the main term on the diagonal, denoted V_{zz} (a second derivative of the electric potential V in the direction of the principal axis of the diagonalized EFG) and the asymmetry parameter (η), defined as

$$\eta = |V_{xx} - V_{yy}|/|V_{zz}|, \tag{1}$$

where V_{xx} and V_{yy} are the two other diagonal terms. These two EFG parameters suffice because the condition $V_{xx} + V_{yy} + V_{zz} = 0$ is maintained due to Laplace's equation $\nabla^2 V = 0$.

In the least-squares fitting of the spectra, the quadrupole coupling constant $e \cdot Q \cdot V_{zz}$ enters the model, giving the strength of the electric hyperfine interaction in energy units (or Doppler-velocity units). In this constant, eQ is the quadrupole moment of the excited state of ^{57}Fe in units of Cm^2. A complication may arise from the fact that the direction of the magnetic field that causes the nuclear Zeeman splitting does not always coincide with the direction of V_{zz}. In such a case, additional parameters need to be determined by fitting; the angles α and β, which fix the direction of $\vec{B}$ with respect to the coordinate system defined by V_{xx}, V_{yy} and V_{zz}.

Calculations of quadrupole coupling constants: The EFG was calculated for two principal charge contributions; from oxygen anions and from ordered orbitals, both approximated as point charges. The matrix of their contribution to EFG was constructed from its individual elements V_{ij} calculated according to Gütlich [15]:

$$V_{ij} = \frac{1}{4\pi\varepsilon_0} \sum_k q_k \left(\frac{3x_i^k x_j^k}{r_k^5} - \frac{\delta_{ij}}{r_k^3} \right), \quad i,j = 1,2,3, \tag{2}$$

where the sum of charges runs over the nearest charges of the given type around the Mössbauer nucleus, ε_0 is the permittivity of the free space, q_k is the k-th nearest charge, and i,j label the three crystallographic directions $1 \equiv a$, $2 \equiv b$, $3 \equiv c$ so that r_k is the distance from Fe to the k-th charge, x_i^k is a coordinate for the k-th charge, and δ_{ij} is the Kronecker delta. Sternheimer anti-shielding and shielding factors [16] were used to correct for the fact that the Mössbauer nucleus sees the EFG through its own core-electron cloud. This correction was applied as $1 - \gamma_\infty = 12.035$ to eQV_{ij} of the contribution from anionic charges and as $1 - \sigma = 0.8854$ to eQV_{ij} of the contribution from orbital charges. For the quadrupole moment of the excited state of ^{57}Fe, $Q = 0.15 \times 10^{-28} m^2$ was used [17] to calculate eQV_{ij} in energy units and then converted into velocity units by multiplying with the "Doppler factor" of the ^{57}Fe resonance, c_0/E_γ, where c_0 is the speed of light and $E_\gamma = 14.37$ keV is the energy of the Mössbauer γ quantum. In this manner, the matrices of the contributions to EFG were evaluated separately for each type of charge contribution, and the quadrupole coupling constant eQV_{zz} was extracted from them by first diagonalizing the eQV_{ij} sum matrix and then picking the largest component of the three diagonal terms eQV_{xx}, eQV_{yy} and

Table 1
Synthesis conditions of $NdBaFe_2O_{5.001(1)}$.

	t/°C	Ar/H_2	log (p_{H_2O}/bar)	log (p_{O_2}/bar)	τ/day
Calcination	900	56(7)	−1.67(1)	−15.98(9)	1
Sintering	1040	16(1)	−1.68(1)	−14.70(3)	4
Oxygen-content control	800	0	−1.65	−21.5	7

Note: Standard errors of the volume ratio Ar/H_2 refer to variations over time τ.

eQV_{zz}. In the end, the total of those two contributions to EFG was calculated for each of the three eQV_{ii} terms.

3. Results and discussion

3.1. Structural characterizations

The refined structure parameters of the two structure types of charge-ordered $RBaFe_2O_5$ at 100 K are listed in Tables 2 and 3 for $R=$Nd and Gd, respectively. Bond-valence sums listed in Table 4 suggest that the long-range ordered separation (as seen by diffraction) of the two unequal iron atoms is 0.55 valence units for $R=$Nd and 0.65 for $R=$Gd when bond-valence parameters of Ref. [18] are used. The refined structure parameters for $R=$Nd at 300 K are in Table 5.

Because the weak Bragg reflections of the valence-ordered superstructure are apparent also on the short isothermal scans, structural data were refined across the two-phase range of the first-order Verwey transition. Fig. 1 shows a very symmetrical sigmoid curve for the contents of the low- and high-temperature phases. This is an improvement from the tailed curves obtained [13] for samples in which the oxygen content was only quenched and not homogenized by subsequent annealing.

The unit cells of $NdBaFe_2O_{5.001}$ at 100 K (charge ordered; $P\,2_1ma$) and 300 K (valence mixed; $Pmmm$) are drawn in Fig. 2. $GdBaFe_2O_5$ differs only in the low-temperature charge-ordered structure, which is of the $Pmma$ space group and lacks the tilting of the Fe-coordination square pyramids shown by the Nd variant.

3.2. Overview of Mössbauer valence- and spin-states in $NdBaFe_2O_5$

3.2.1. Antiferromagnetic state

Mössbauer spectra typical of the valence-mixed, premonitory-ordered and charge-ordered states in $NdBaFe_2O_5$ are shown in Fig. 3. Magnetic ordering is apparent from the typical sextets, the

Table 4
Bond-valence sums for metals in charge-ordered $NdBaFe_2O_{5.001}$ and $GdBaFe_2O_{5.009}$ at 100 K, calculated from data in Tables 2 and 3.

Atom	$NdBaFe_2O_{5.001}$	$GdBaFe_2O_{5.009}$
R	2.96(4)	2.88(2)
Ba	2.03(2)	1.99(1)
Fe(1)	2.78(6)	2.88(3)
Fe(2)	2.23(4)	2.23(2)

Table 2
Structure parameters for charge-ordered $NdBaFe_2O_{5.001}$ at 100 K.

Unit cell				Refinement statistics		
Space group		$P\,2_1ma$		R_{wp}		0.1080
a (Å)		8.01703(1)		R_p		0.0765
b (Å)		3.91984(1)		$R(F^2)$		0.0332
c (Å)		7.63395(1)		N_{obs}		1508
V (Å³)		239.900(1)		$N_{variables}$		32

Atom	Site	x	y	z	$100U_{iso}$[a]
Nd	2a	0.0090(1)	0	0.4916(1)	0.18(1)
Ba	2a	0	0	0.0028(1)	0.18(1)
Fe(1)	2b	0.2649(3)	1/2	0.2514(3)	0.10(1)
Fe(2)	2b	0.7555(3)	1/2	0.2659(2)	0.10(1)
O(1)	2b	0.2368(6)	1/2	0.0019(10)	0.36(3)
O(2a)	2a	0.7540(10)	0	0.3041(10)	0.36(3)
O(2b)	2a	0.2632(10)	0	0.3040(10)	0.36(3)
O(3a)	2b	0.0155(11)	1/2	0.2936(5)	0.36(3)
O(3b)	2b	0.5009(12)	1/2	0.3132(5)	0.36(3)

[a] In Å²; constrained equal for Nd and Ba, both irons and for all oxygens.

Table 3
Structure parameters for charge-ordered $GdBaFe_2O_{5.009}$ at 100 K.

Unit cell				Refinement statistics		
Space group		$Pmma$		R_{wp}		0.1014
a (Å)		8.07405(1)		R_p		0.0736
b (Å)		3.86019(1)		$R(F^2)$		0.0622
c (Å)		7.56552(1)		N_{obs}		1505
V (Å³)		235.797(1)		$N_{variables}$		23

Atom	Site	x	y	z	$100U_{iso}$[a]
Gd	2c	0	0	1/2	0.13(1)
Ba	2a	0	0	0	0.29(1)
Fe(1)	2f	1/4	1/2	0.2507(1)	0.14(1)
Fe(2)	2f	3/4	1/2	0.2688(1)	0.14(1)
O(1)	2f	1/4	1/2	0.0011(9)	0.40(3)
O(2a)	2e	3/4	0	0.3133(8)	0.40(3)
O(2b)	2e	1/4	0	0.3106(8)	0.40(3)
O(3)	4j	0.0097(5)	1/2	0.3076(2)	0.40(3)

[a] In Å²; constrained equal for both irons and for all oxygens.

Table 5
Structure parameters for valence-mixed $NdBaFe_2O_{5.001}$ at 300 K.

Unit cell				Refinement statistics	
Space group	$Pmmm$			R_{wp}	0.1116
a (Å)	3.97378(1)			R_p	0.0802
b (Å)	3.96243(1)			$R(F^2)$	0.0450
c (Å)	7.64601(1)			N_{obs}	594
V (Å³)	120.393(1)			$N_{variables}$	22

Atom	Site	x	y	z[a]	$100U_{iso}$[b]
Nd	2a	0	0	0.5	0.67(1)
Ba	2a	0	0	0	0.67(1)
Fe	2b	1/2	1/2	0.2597(1)	0.63(1)
O(1)	2b	1/2	1/2	0	0.93(5)
O(2)	2a	1/2	0	0.3039(2)	0.93(5)
O(3)	2b	0	1/2	0.3039(2)	0.93(5)

[a] Constrained equal for O(2) and O(3).
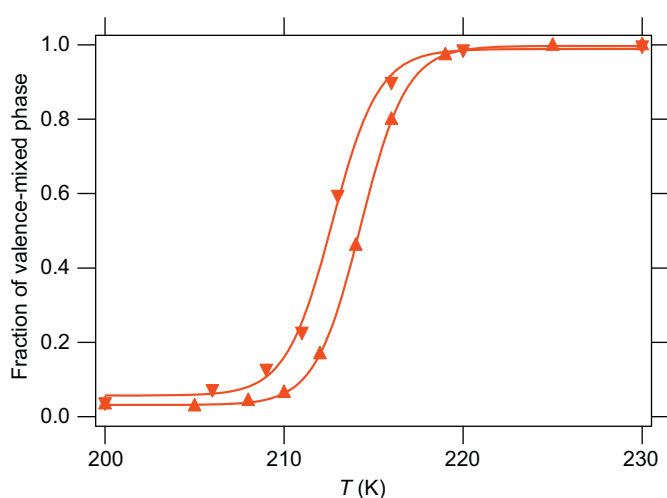[b] In Å²; constrained equal for Nd and Ba and for all oxygens.

Fig. 1. Hysteresis at Verwey transition of $NdBaFe_2O_{5.001}$ from Rietveld refinements of SXPD data. Points are fitted by symmetrical sigmoid curves.

span of which is proportional to the internal magnetic field B at the nucleus, while their relative shift characterizes the valence state (the isomer shift). As determined previously [4], the ordered spin moments of iron in $NdBaFe_2O_5$ are oriented along b and coupled antiferromagnetic (AFM) except for the direct Fe–Fe interaction across the Nd layer which is ferromagnetic and remains so at all temperatures below T_N. For all the other variants, this interaction turns AFM below T_V [4]. As will be discussed in Section 3.5, the Mössbauer nucleus sees each spin moment as having correct relative magnitude yet inverted orientation.

The valence-mixing sextet $^{CN5}Fe_{VM}^{2.5+}$ is observed with an isomer shift of ~ 0.6 mm/s and hyperfine parameters compatible with the pentacoordinated (CN5) iron–oxygen network. As in Ref. [6], the slight asymmetry in the height and width of lines 1 and 6 is modeled by considering two very similar valence-mixed components: $^{CN5}Fe_{VM1}^{2.5+}$ and $^{CN5}Fe_{VM2}^{2.5+}$. The internal field is about 30 T. The premonitory ordering is characterized by the appearance of two partially separated valence states of iron, $Fe^{>2.5+}$ and $Fe^{<2.5+}$, as manifested by both isomer shift and diverging internal fields. The charge ordering accomplishes the separation of charges into $^{CN5}Fe_{2O\,T,CO}^{2+}$ and $^{CN5}Fe_{5O\,T,CO}^{3+}$ with the internal fields of 20.6 T and 51.8 T (at 77 K) rounded off in the symbol. Other components are weak. Because they are associated with defects in valence mixing and charge ordering, these weak components will be discussed together with the effect of the oxygen nonstoichiometry.

3.2.2. Paramagnetic state

At 448 K, some 15–20° above the Néel temperature [4], the Mössbauer spectrum (Fig. 4) is dominated by a single line showing neither electric quadrupole nor magnetic interaction. The isomer shift of ~ 0.45 mm/s relative to α–Fe suggests that the Fe atoms are still in the valence-mixed state of $Fe^{2.5+}$. In addition, a small doublet due to Fe^{3+} and possibly a singlet due to Fe^{2+} are seen. It should be noted that our Mössbauer samples at this temperature (175 °C) eventually started showing magnetic lines that grew as a function of time; a sign of thermally induced oxidative decomposition of the main phase facilitated by the limited thermal stability of the epoxy holders.

3.3. Mössbauer parameters affected by lower symmetry of $NdBaFe_2O_5$

The symmetry lowering of the charge-ordered $NdBaFe_2O_5$ as compared with the Sm–Ho variants makes a profound difference for two Mössbauer parameters that both concern the divalent iron state $^{CN5}Fe_{2O\,T,CO}^{2+}$: Its internal field is more than two times larger, and the quadrupole-coupling constant is about two times smaller. As the lower symmetry provides spectral features needed for a more accurate fitting of Mössbauer parameters, separate Section 3.5 and 3.6 are devoted to interpretation of these anomalies.

3.4. Mössbauer isomer shift

In Fig. 5, isomer-shift values for $NdBaFe_2O_5$ are plotted as a function of temperature and compared on a unit-valence scale assigned to isomer shifts 0.992 and 0.418 mm/s obtained previously [6] for $EuBaFe_2O_5$ at 77 K. The data in Fig. 5 suggest that the valence separation at 77 K in the charge-ordered $NdBaFe_2O_5$ is 80% of that for $GdBaFe_2O_5$.

3.5. Mössbauer internal field

As illustrated in Fig. 6, the internal field for divalent iron in charge-ordered $NdBaFe_2O_5$ is 20.6 T at 77 K, hence much higher than 7.5 T seen [2,6,19] for the other R variants. Such a low field for what neutron powder diffraction [2,4] sees as a high-spin AFM Fe^{2+} with magnetic moments along b has been explained in
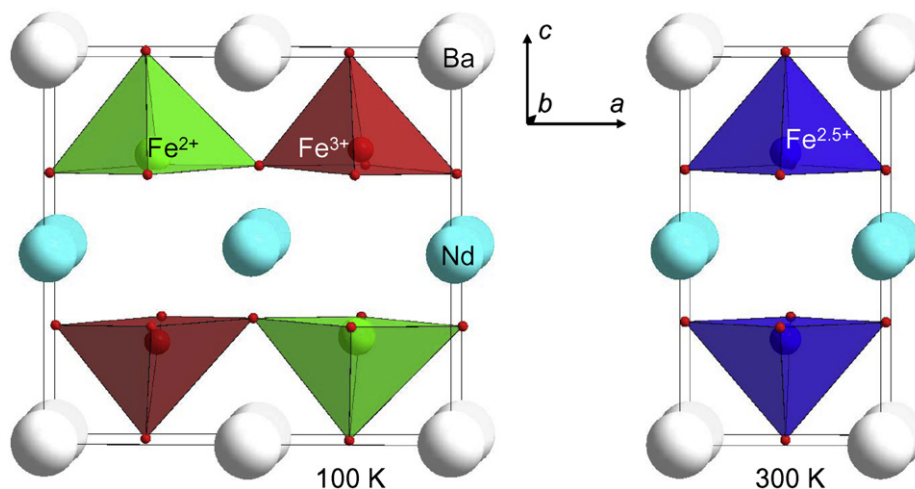
Fig. 2. Unit cells of NdBaFe$_2$O$_{5.001}$ as charge ordered (100 K; $P2_1ma$) and valence mixed (300 K; $Pmmm$).

Ref. [2] in terms of the Mössbauer nucleus experiencing the spin and orbit magnetic moment differently than neutron diffraction. In more detail than in Ref. [2]: The Fermi contact interaction via s electrons makes the nucleus see the electron spin with inverted sign. On the other hand, the angular momentum of the electron is not inverted. The Mössbauer nucleus therefore experiences the Russell–Sounders coupling as L−(−S) for a less than half-filled d shell and L+(−S) for a more than half-filled d shell, such as Fe^{2+}.

The expected spin-only internal field of Fe^{2+} in RBaFe$_2$O$_5$ is estimated as 4/5 of the L = 0 field 51.8 T of Fe^{3+}, yielding B_S = 41.4 T at 77 K. In the charge-ordered R= Sm–Ho variants of this phase, the orbit (angular-momentum) contribution, B_L, is so strong that it decreases the total to B=7.5 T. In contrast, the normal "disordered" Fe^{2+} component (which does not participate in the charge ordering) has $B \approx 27$ T [6]. The enhancement of B_L for the charge-ordered Fe^{2+} must originate in the orbital ordering of d_{xz}, which is the only differing feature from the normal Fe^{2+}. The orbital ordering is manifested by the orthorhombic distortion [4], which is accordingly smaller for NdBaFe$_2$O$_5$. Also the symmetry lowering to $P2_1ma$ [4] makes the orbital ordering less favorable in NdBaFe$_2$O$_5$; both factors decreasing B_L, hence increasing the total B (to 20.6 T at 77 K).

What is the role of the ordered Fe^{2+} d_{xz} orbital in producing the strong B_L? A doubly occupied orbital contributes with zero S and zero L. Neither would a separate, non-degenerate, t_{2g} orbital produce a non-zero B_L. The angular-momentum contribution comes from the other two t_{2g} orbitals, d_{xy} and d_{yz}, which are necessarily also ordered and have the common rotation axis b that produces B_L along this direction. Each of them is occupied with a single majority-spin electron, and crystal-field calculations in Section 3.6.1 show that they are practically degenerate. The expectation value of the angular momentum per majority electron is $\langle \frac{1}{2}(d_{xy}+d_{yz})|L_y|\frac{1}{2}(d_{xy}+d_{yz})\rangle = \hbar$, hence $2\hbar$ in total along b. The Russell–Sounders coupling will keep L parallel with the alternating (AFM) orientation of S, and, as explained above, the Fe nucleus will see these spin and orbit contributions as antiparallel.

3.6. Mössbauer quadrupole interaction

The temperature evolution of the quadrupole coupling constants is shown in Fig. 7. Numerical values for significant temperatures are listed in Table 6.

For charge-ordered Fe^{2+} in NdBaFe$_2$O$_5$, the highly asymmetrical sextet of the spectral component ^{CN5}Fe$^{2+}_{20\,T,CO}$ (Fig. 3c) yields

a large quadrupole coupling constant eQV_{zz} = 1.91 mm/s whereas an even larger eQV_{zz} = 3.87 mm/s is fitted from the spectra of GdBaFe$_2$O$_5$ (Table 6) and other R variants [2,6,8,19]. The angle between V_{zz} and $\vec{B}$ is fitted to zero, which means that the main component of the EFG at the Fe nucleus, V_{zz}, is parallel to the base of the square-pyramidal coordination (along b) for all R including Nd, hence not pointing away from the apical oxygen (along c) as would be expected from the ligand-charge configuration. As was the case of the internal field, orbital ordering is the explanation we suggest and discuss in Section 3.6.1 for this anomaly in magnitude and orientation of the EFG: In order to obtain correct EFG, electron charges of the ordered doubly occupied orbital need to be considered together with the charges of the oxygen ions.

Orbital charges of Fe^{3+} cancel by symmetry, and its EFG is controlled by its ligand-charge constellation. In both NdBaFe$_2$O$_5$ and GdBaFe$_2$O$_5$, the rather symmetrical sextet of the spectral component ^{CN5}Fe$^{3+}_{50\,T,CO}$ in Fig. 3c corresponds to a relatively small quadrupole coupling (Table 6). Obtaining both its magnitude and orientation from least-squares fitting to the spectrum poses a challenge; an equally good fit is obtained upon a mere change in the V_{zz} sign, which leads to a new orientation (angle β), as listed in Table 6. This dichotomy of the V_{zz} sign and orientation is typical for highly symmetrical sextets of low eQV_{zz}/B ratio. For asymmetrical sextets, such as those of charge-ordered Fe^{2+}, this problem does not occur and even the angle β can be refined with a high precision. While the fitted EFG data for Fe^{3+} in GdBaFe$_2$O$_5$ are not ambiguous because only the alternative of the positive V_{zz} oriented along c (Table 6) is expected from the configuration of the anion charges around Fe^{3+}, the two alternatives for NdBaFe$_2$O$_5$ have either an unexpected sign or an unexpected orientation. This ambiguity is also addressed in the Section 3.6.1 that follows.

3.6.1. Simulations of quadrupole coupling constants in charge-ordered state

Quadrupole coupling constants of the EFG due to charges of the nearest oxygen anions (ligand contribution, V_{ij}^{ligand}) and due to the sixth d electron located in the doubly occupied ordered d_{xz} orbital (Fe^{2+}) (orbital-ordering contribution, V_{ij}^{OO}) were calculated from atomic coordinates in Tables 2 and 3, as described in Section 2. The point charges q_k in Eq. (2) and the orientations of the main component of the EFG were estimated as follows:

For the ligand contribution, $-0.93e$ at each of the five oxygen sites is the charge that produces the c-parallel, ligands-only, eQV_{zz}=0.7 mm/s value for Fe^{3+} in GdBaFe$_2$O$_5$ obtained by fitting

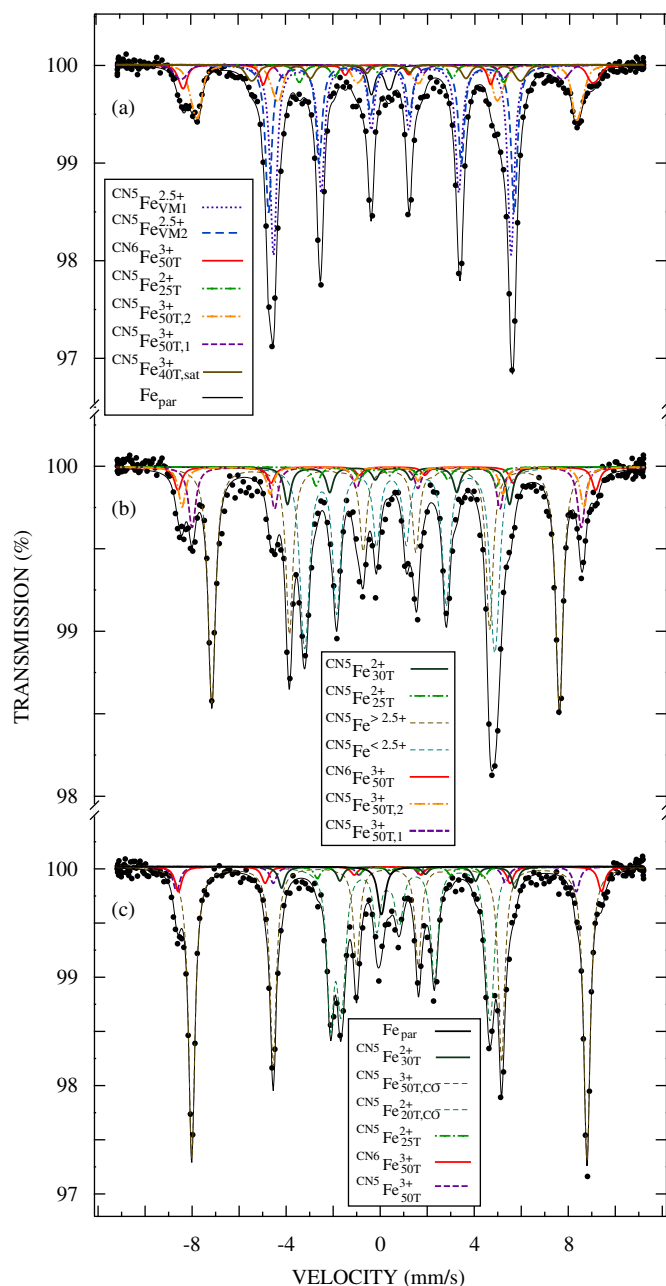**Fig. 3.** Mössbauer spectra of NdBaFe$_2$O$_{4.997}$, recorded for (a) valence-mixed phase at 300 K, (b) the premonitory-ordered phase at 240 K, (c) the charge-ordered phase at 77 K. Spectral components used in the fitting are identified in the legend.

Fig. 4. Paramagnetic Mössbauer spectrum of NdBaFe$_2$O$_{5.001}$ recorded at 448 K.

Fig. 5. Temperature evolution of the Mössbauer isomer shift for NdBaFe$_2$O$_{4.997}$ on a valence scale relative to the other R variants from Ref. [6]. For comparison, data obtained for GdBaFe$_2$O$_{5.019}$ [19] and GdBaFe$_2$O$_{5.010}$ (this work) are shown in gray open symbols. Correction for the second-order Doppler shift due to temperature difference δ_T from 77 K is applied as $\delta_T = 7 \times 10^{-4} \Delta T$ mm/s.

the eQV_{zz} temperature dependence in Fig. 7. In other words, we set GdBaFe$_2$O$_5$ as our standard for the trivalent charge-ordered iron of no orbital-ordering contribution to EFG.

For the d_{xz} orbital-ordering contribution at Fe^{2+} in GdBaFe$_2$O$_5$, $-0.08e$ at each of the four orbital lobes at a chosen fixed distance $l=0.3$ Å from the iron nucleus (Fig. 8) is the charge that complements the calculated ligand contribution at charge-ordered Fe^{2+} to the observed total EFG listed in Table 6. Both the charge and the orientation along b of the main component of the orbital-ordering contribution to EFG are unambiguous; the charge because l and the charge are not independent and correlate as a factor of $\sim q/l^3$, the orientation owing to the asymmetry of the Mössbauer spectrum of the divalent component. The two remaining directional components of the orbital-ordering
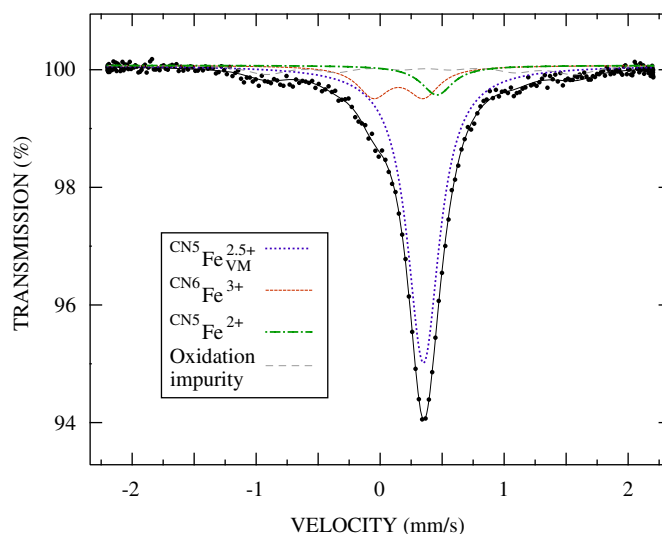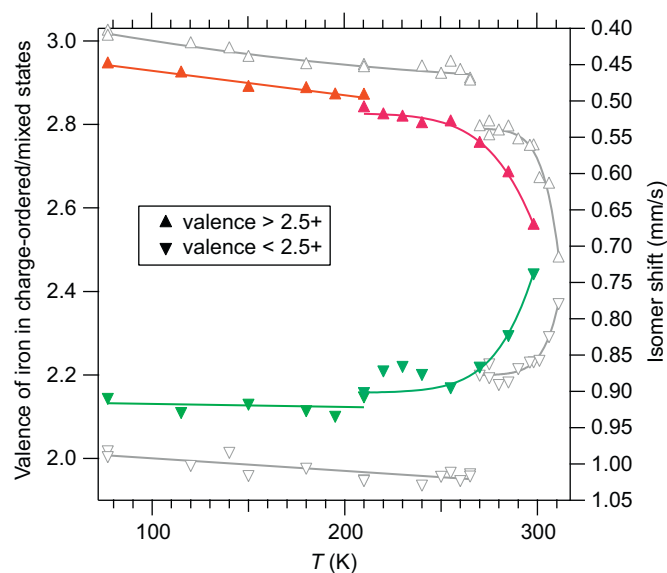
contribution to EFG are equal because of fourfold symmetry and can be chosen in the ac plane.

For NdBaFe$_2$O$_5$, an analogous procedure produced a charge of $-0.048e$, suggesting a less complete orbital- and charge-ordering in accordance with the small orthorhombic distortion [3,5] and the isomer shift in Fig. 5, while the orientation remained along b as for GdBaFe$_2$O$_5$. The thus implied partial Fe^{3+} presence at the divalent charge-ordered site, Fe(2), is mirrored by a partial (local or temporal) Fe^{2+} presence at the trivalent site, Fe(1), in the structure. Consequently, a small charge of $-0.007e$ of the minority-spin electron at each of the four d_{xz} lobes around the trivalent site was estimated as one that produces an orbital-ordering contribution to EFG of 0.4 mm/s along b, estimated as 4.79×0.08, where 4.79 mm/s is our simulated orbital-ordering contribution to EFG in GdBaFe$_2$O$_5$ assigned to a full orbital order, and 0.08 is the Fe^{2+} concentration on the trivalent iron site at 77 K, read out from Fig. 5. While the charge estimate is final, the
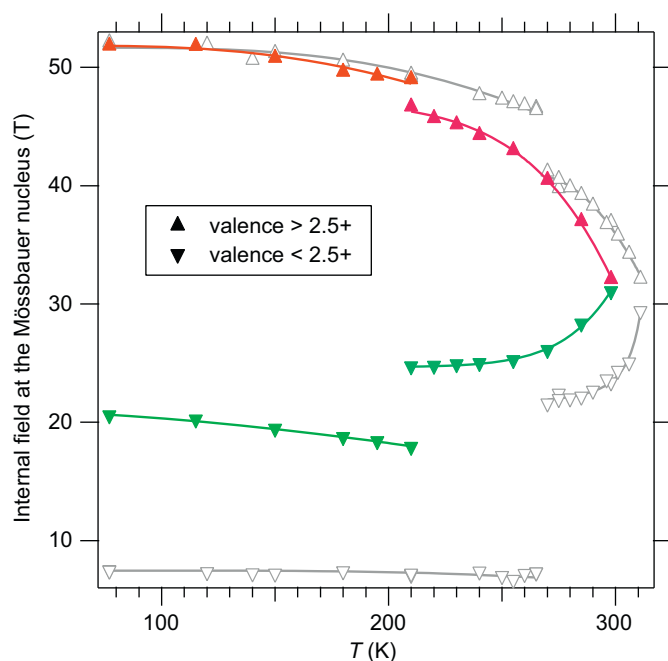
Fig. 6. Internal fields of the two main components of Mössbauer spectra of NdBaFe$_2$O$_{4.997}$ at various temperatures. For comparison, data obtained for GdBaFe$_2$O$_{5.019}$ [19] and GdBaFe$_2$O$_{5.010}$ (this work) are shown in gray open symbols. Note that the transition temperatures are different for the Nd and Gd versions of the phase.
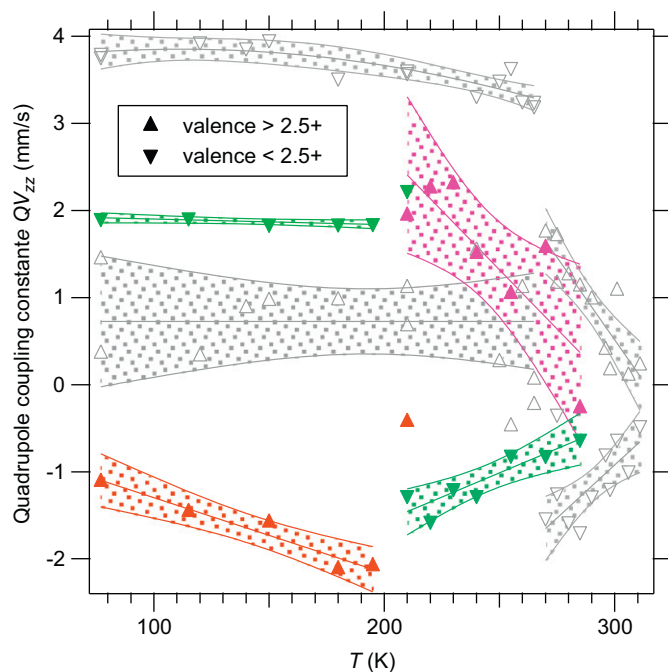

Fig. 7. Temperature evolution of the quadrupole coupling constants for main components in Mössbauer spectra of NdBaFe$_2$O$_{4.997}$, with 95% confidence fields drawn for the temperature dependences. For comparison, data obtained for GdBaFe$_2$O$_{5.019}$ [19] and GdBaFe$_2$O$_{5.010}$ (this work) are shown in gray open symbols.

Table 6

Average of fitted parameters eQV_{zz} (in mm/s), η and angle β between V_{zz} and $\vec{B}$ for the following Mössbauer components in RBaFe$_2$O$_5$: charge ordered at 77 K, intermediate right above T_V, valence mixed right above T_P.

R	Valence	eQV_{zz}	η	β
Nd	Fe^{2+}	1.92(6)	0.5(2)	0(2)°
Gd	Fe^{2+}	3.82(20)	0.4(2)	0(10)°
Nd	Fe^{3+}	−1.10(31)	0.75(5)	75(8)°
		or 0.15(4)	0.4(1)	0° [a]
Gd	Fe^{3+}	0.7(8)	0.7(1)	90° [a]
		or −0.06(2)	0.6(2)	0° [a]
Nd	Fe$^{<2.5+}$	−1.46(26)	0.5(2)	90° [a]
Gd	Fe$^{<2.5+}$	−1.65(37)	0.1(2)	90° [a]
Nd	Fe$^{>2.5+}$	2.4(9)	0.8(2)	90° [a]
		or −0.34(8)	0.95(10)	0° [a]
Gd	Fe$^{>2.5+}$	1.65(38)	0.6(1)	90° [a]
		or −0.3(1)	0.6(1)	0° [a]
Nd	Fe$^{+2.5}$	−0.2	0 [b]	90° [a]
		or positive		and 0°
Gd	Fe$^{+2.5}$	−0.3	0 [b]	90° [a]
		or positive		and 0°

The eQV_{zz} error bars in brackets are the widest half-width of the 95% confidence intervals (belts) in Fig. 7, other error bars are estimated.

[a] Fixed because refining both the EFG magnitude and angle gave unstable refinement while the angle was not changing significantly.
[b] Not refinable because quadrupole coupling is nearly absent due to symmetry.

symmetry-induced dichotomy of the EFG magnitude and orientation allows the main component V_{zz} to be either negative and perpendicular to b or positive and parallel to it (Table 6). Of these two alternatives, only the negative V_{zz} perpendicular to b is compatible with both the ligand contribution and the above estimate of orbital-ordering contribution, which, interestingly, produce together a term dominating along the a axis (Table 7).

The results of the EFG simulations are summarized in Table 7. For sake of numerical agreement under summations, the EFG estimates are given with two decimals, regardless of standard deviations. In general, one can say that the implied main directions of the total EFG are robust, and only huge changes in the charge magnitudes would change the EFG components enough to switch the total EFG direction to another one.

Let us illustrate the data in Table 7 with Fe^{2+} of NdBaFe$_2$O$_5$. Here the strongest ligand contribution to EFG is 1.08 mm/s, 37.8° away from c, which is due to the tilt of the coordination square pyramid. The second strongest ligand contribution is along b, with magnitude $(1-\gamma_\infty)eQV_{yy}^{\text{ligand}} = -0.77$ mm/s nearly as large as the first one owing to the strong local orthorhombic distortion. Fig. 8 shows how the charge of the ordered d_{xz} orbitals (Table 7) is able to turn the main total EFG component to being parallel with $\vec{B}$; in agreement with the experimental data in Table 6 where their angle $\beta = (0 \pm 2)°$. Fig. 9 shows an analogous situation for the Sm–Ho variants where the measured (main total) Fe^{2+} EFG component increases due to the increased orbital ordering in these phases. For our GdBaFe$_2$O$_5$ reference phase, the main total EFG estimate in Table 7 is of course identical with the experimental +3.82(20) mm/s in Table 6 and the calculated asymmetry parameter $\eta = 0.43$ agrees with 0.4(2) in Table 6.

For Fe^{3+} of NdBaFe$_2$O$_5$, the strongest component of the calculated ligand contribution to EFG appears at 30° to c (0.87 mm/s, Table 7) due to the tilting of the coordination square pyramid. The second strongest contribution equals −0.52 mm/s. When summed with the orbital-ordering contribution, it is this value that makes the total EFG component of Fe^{3+} negative and directed preferentially along a, as suggested by the fit of the spectrum, considering that the $\sim 90°$ angle β between V_{zz} and $\vec{B}$ is close to the observed 75° in Table 6. The deviation in the angle might either indicate canting of the ordered spins (difficult to
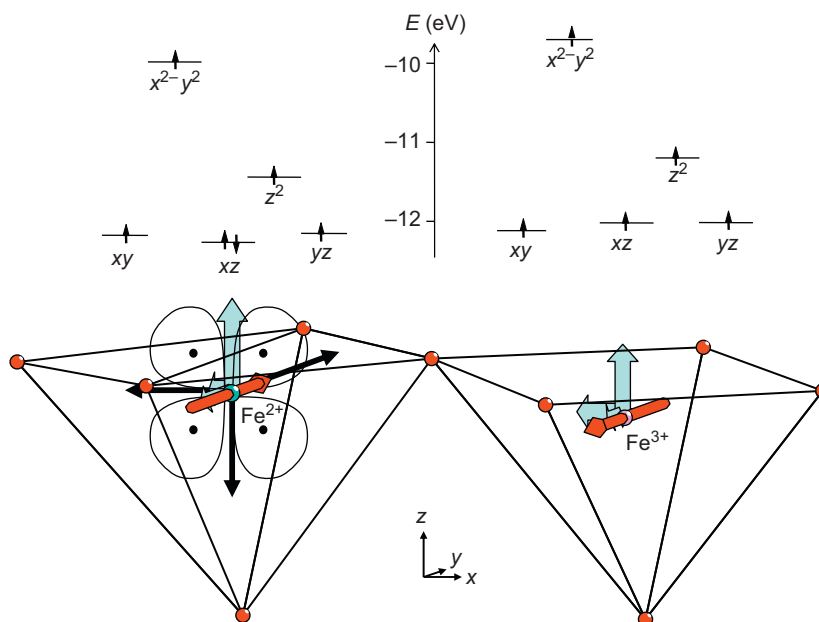
Fig. 8. Sketch of the local EFG ligand components (broad arrows), orbital-ordering components (black arrows) and spins (rod-like arrows) in charge-ordered NdBaFe$_2$O$_5$. The simplified point-charge distribution used for the simulation of V_{ij}^{OO} is shown as black dots inside d_{xz} lobes. Orbital energies are calculated by Caesar 2.0 [14] from structural data in Table 2.

Table 7

Calculated EFG at the two iron sites in charge-ordered RBaFe$_2$O$_5$ for $R=$Nd and Gd at 77 K: magnitudes (mm/s) and angular tilts (if non-zero) of directional components for the ligand contribution $(1-\gamma_\infty)eQV_{ii}^{ligand}$ and orbital-ordering (OO) contribution $(1-\sigma)eQV_{ii}^{OO}$.

$R=$Nd	Nearly divalent iron site			Nearly trivalent iron site		
Direction	OO	Ligand	Total	OO	Ligand	Total
a	−1.35	−0.31, 37.8°	−1.66	−0.20	−0.52, 30.1°	**−0.72**
b	**+2.69**	−0.77	**+1.92**	**+0.40**	−0.35	+0.05
c	−1.35	**+1.08**, 37.8°	−0.26	−0.20	**+0.87**, 30.1°	+0.67

$R=$Gd	Divalent-iron site			Trivalent-iron site		
Direction	OO	Ligand	Total	OO	Ligand	Total
a	−2.40	−0.25	−2.65	0	−0.35	−0.35
b	**+4.79**	−0.97	**+3.82**	0	−0.35	−0.35
c	−2.40	**+1.22**	−1.17	0	**+0.70**	**+0.70**

The dominating OO-, ligand-, and total EFG contributions are boldfaced.

refine from neutron powder diffraction data), but more likely it is an artifact of fitting the weak EFG features of the trivalent Mössbauer component.

At this point it is apparent that the orbital ordering at Fe^{2+} is behind several features of the Mössbauer spectra of charge-ordered RBaFe$_2$O$_5$ at low temperatures. It controls both the EFG and the orbit contribution B_L, from both of which it can be evaluated and crosschecked. Evaluation from the EFG concerns directly the charge of the ordered orbital. As an example, the necessity to decrease the ordered charge n from 0.08 for the Gd variant to 0.048 for the Nd variant can be interpreted such that the orbital ordering in NdBaFe$_2$O$_5$ is 60% ($=0.048/0.08$) of the ordering in the Sm–Ho variants. The same percentage follows from the orbital-ordering contribution to the internal field: the orbit contribution of Fe^{2+} in NdBaFe$_2$O$_5$ is $B_L= B_S-B=(41.4-20.6)=$ 20.8 T (Section 3.5), which is $\sim$60% of the orbit contribution of $(41.4-7.5)$ T = 33.9 T for the Sm–Ho versions.

Having established a small orbital-ordering contribution to the EFG also at Fe$_{CO}^{3+}$ in NdBaFe$_2$O$_5$ as a consequence of a less complete charge separation, it is interesting to see whether such an increased presence of divalent iron could bring an orbit contribution B_L to the internal field at the trivalent site Fe(1) (Table 2). Experimental data [6,19] show that the internal field of Fe$_{CO}^{3+}$ is practically the same for the entire Ho–Nd series of this phase. The NdBaFe$_2$O$_5$ B value is only slightly lower (Fig. 6), which is fully explainable by the less complete charge separation: With an Fe^{2+} concentration of 0.08 at the "trivalent" component (Fig. 5), the S-only decrease is 0.04 of 5/2, corresponding to a field 51.0 T instead of 51.8 T, providing no room for an eventual L contribution. Why does not Fe^{2+} at the trivalent site yield any B_L? For the divalent iron at its own charge-ordered site, the B_L contribution is not due to the minority electron but arises because the d_{xy} and d_{yz} orbitals are degenerate and form the $\frac{1}{2}(d_{xy}+d_{yz})$ state. According to crystal-field calculations (Fig. 8), these orbitals are not degenerate at the Fe$_{CO}^{3+}$ site.

3.6.2. Quadrupole coupling constants in the valence-mixed state

The two separated iron states are disordered in the temperature interval $T_V < T < T_p$, and structural data are therefore not available. However, warming through T_p produces a simple structure with one square-pyramidal coordination of iron. Only a tiny orthorhombic distortion prevents it from having tetragonal symmetry (Table 5, Fig. 2). Yet, instead of the expected positive quadrupole coupling constant of $\sim$1 mm/s corresponding to this constellation of charges, the fitted value is small and negative (-0.27 mm/s, Table 6) when the angle between V_{zz} and $\vec{B}$ is correctly set to $\beta=90°$. The sign changes to being positive only when a wrong angle $\beta=0°$ is fixed, but the constant remains too small.

The experimental quadrupole coupling constant is modeled well only when a fractional charge is added to the Fe coordinations along c. As an example, adding a charge of about $-e/3$ halfway between the two ferromagnetic valence-mixing Fe atoms reproduces the experimental value of -0.27 mm/s. A more refined solution is based on the recent density-functional theory calculations [20], which suggest that the valence-mixing electron in
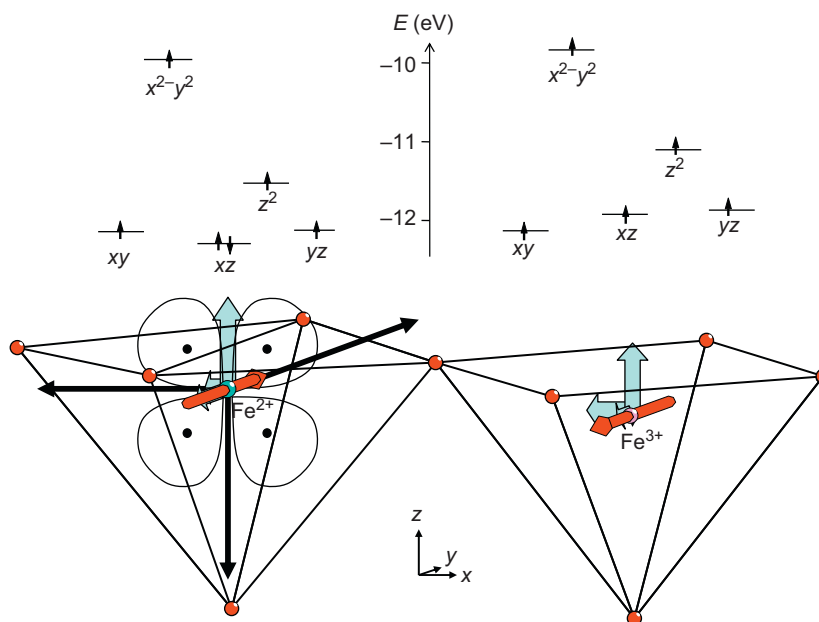
Fig. 9. Sketch of the local EFG ligand components (broad arrows), orbital-ordering components (black arrows) and spins (rod-like arrows) in charge-ordered $GdBaFe_2O_5$. The simplified point-charge distribution used for the simulation of V_{zz}^{OO} is shown as black dots inside d_{xz} lobes. Orbital energies are calculated by Caesar 2.0 [14] from structural data in Table 3.

$YBaFe_2O_5$ occupies mainly the d_{z^2} orbital. The electron is shared between the d_{z^2} orbitals of the two Fe sites facing each other along the c axis, with some occupation also at $d_{x^2-y^2}$. These two e_g orbitals would not produce any contribution to B_L, but the V_{zz}^{OO} contribution can be easily estimated. By applying a similar point-charge model as for d_{xz}, it is readily seen that d_{z^2} produces a large negative V_{zz}^{OO} along the c axis and hence positive V_{xx}^{OO} and V_{yy}^{OO} terms equal to each other. Combined with the positive ligand contribution $(1-\gamma_\infty)eQV_{zz}^{ligand} = 0.93$ mm/s along the c axis, the net effect could indeed be a small negative eQV_{zz} along c. In order to make a quantitative estimate of the V_{zz}^{OO} contribution, we included also the minority-spin occupation of $d_{x^2-y^2}$ as calculated in Ref. [20]. It produces a positive V_{zz}^{OO} along the c axis and negative V_{xx}^{OO} and V_{yy}^{OO} terms, i.e., exactly opposite to the d_{z^2} contribution. Due to similar constellation of charges, the $d_{x^2-y^2}$ contribution resembles the ligand contribution. Using the calculated [20] minority-spin charges of 0.390 and 0.138 for the respective d_{z^2} and $d_{x^2-y^2}$ orbitals, we estimate $eQV_{zz} = (1-\gamma_\infty)eQV_{zz}^{ligand} + (1-\sigma)eQV_{zz}^{OO}(-0.390+0.138)$, which, upon inserting $(1-\gamma_\infty)eQV_{zz}^{ligand} = 0.93$ mm/s and $(1-\sigma)eQV_{zz}^{OO} = 4.79$ mm/s, gives $eQV_{zz} = -0.28$ mm/s in agreement with experiment. Note that this estimate assumes that the fully occupied d_{z^2} orbital would contribute with $(1-\sigma)eQV_{zz}^{OO} = -4.79$ mm/s, i.e. equal in magnitude but the opposite to d_{xz}, hence the negative sign in front of the 0.390 charge.

This means that Mössbauer spectroscopy actually sees the valence-mixing electron. Its presence on the d_{z^2} orbital might seem somewhat surprising given the outcome of the Caesar 2.0 [14] orbital-energy calculations for the square-pyramidal cluster suggesting that the energy of the d_{z^2} orbital is well above the t_{2g} levels. However, these Hückel-type calculations do not involve electron–electron interactions and neither the mixing electron nor the magnetic coupling could be included.

3.7. Effect of oxygen nonstoichiometry on valence mixing

In Fig. 10, the relative intensity of the valence-mixed Mössbauer component $Fe^{2.5+}$ in $NdBaFe_2O_{5+w}$ is plotted against w and fitted
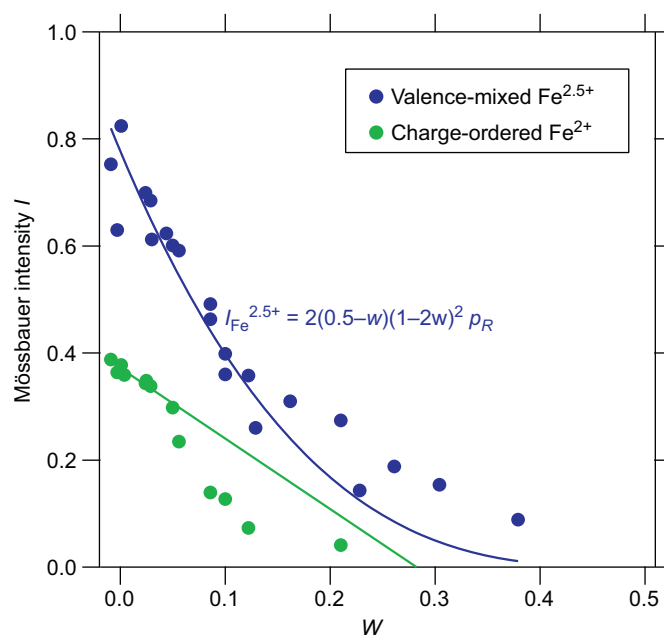

Fig. 10. Fraction of valence-mixed $Fe^{2.5+}$ ($I_{Fe^{2.5+}}$) and charge-ordered Fe versus w in $NdBaFe_2O_{5+w}$ at room temperature, fitted by the scaled function of the probability of mixing of integer valence states.

with the function $I_{Fe^{2.5+}} = 2(0.5-w)(1-2w)^2 p_R$ derived in Ref. [21]. This function describes the probability of mixing between the minority and majority valence state under valence trapping by the oxygen defect at the normally vacant site across the double pyramidal slab in both directions from the candidate valence-mixing pair. The concentration of $Fe^{2.5+}$ decreases similarly as observed for $R = $ Sm [8] and Eu [6], but the function is scaled down. The scaling parameter represents the $Fe^{2.5+}$ concentration in the phase of zero nonstoichiometry w. For $NdBaFe_2O_5$, $p_R = 0.78(2)$, which is 84% of the value found [6] in $EuBaFe_2O_5$. The less favorable valence mixing can be associated with the large size of Nd that separates the Fe sites that mix their valences.

Given the lowered concentration of $Fe^{2.5+}$ in $NdBaFe_2O_5$, the concentrations of the valence, spin, and coordination states of iron that represent defects in the valence mixing are relatively high and better resolved in the Mössbauer spectrum (Figs. 3a and 11). It is possible to discern that the pentacoordinated trivalent iron that failed to mix is composed of twins, $^{CN5}Fe^{3+}_{50T,1}$ and $^{CN5}Fe^{3+}_{50T,2}$ that model better some details on the flanks of the spectrum. This could be just a modeling artifact, but it is not difficult to imagine that two preferred configurations exist for the trivalent-iron square pyramids that failed to mix in the sea of valence-mixed $Fe^{2.5+}$. The remaining valence-mixing defects induced by the oxygen nonstoichiometry w are the previously identified [2,6,8] divalent component $^{CN5}Fe^{2+}_T$, the satellite trivalent component $^{CN5}Fe^{3+}_{40T,sat}$, the occurrence of which was explained in Ref. [8] by the competition to mix the valences, and the component $^{CN6}Fe^{3+}_{50T}$ of concentration practically equal to w as expected.
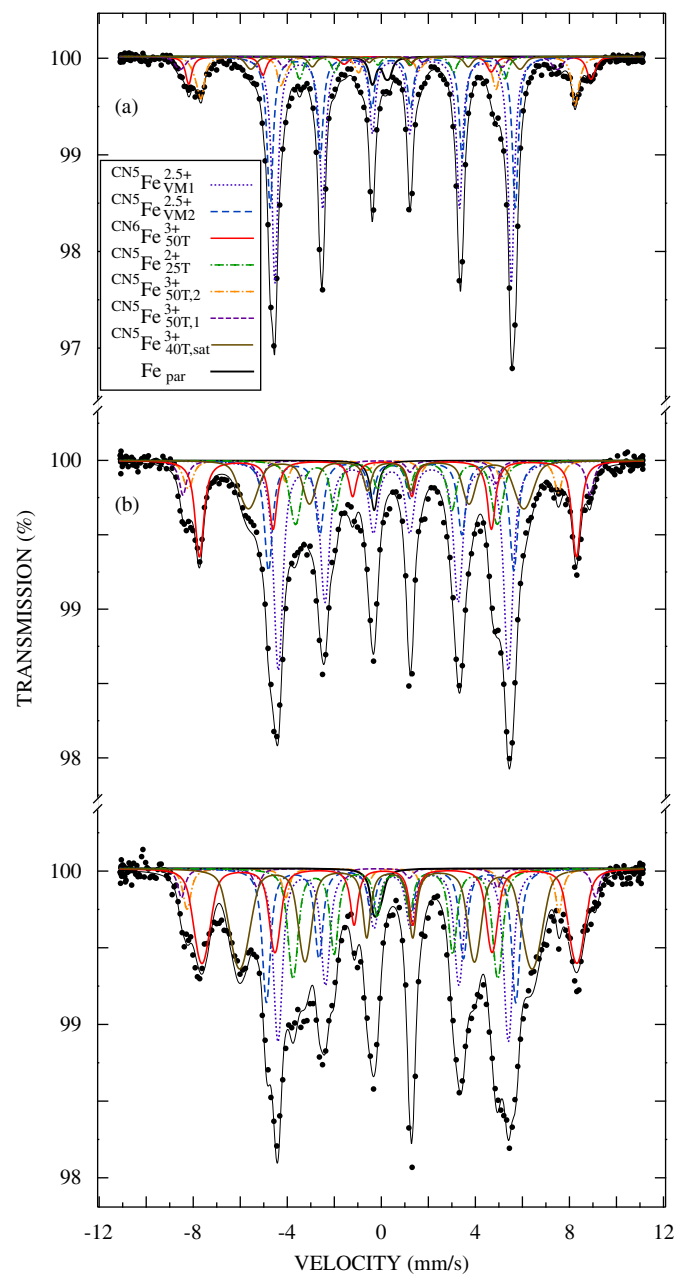

Fig. 11. Mössbauer spectra of $NdBaFe_2O_{5+w}$ at 300 K: (a) $w=0.024$, (b) $w=0.086$, and (c) $w=0.100$. Components used in the fitting are identified in the legend.

In addition to the di- and trivalent defects, spectra in Fig. 11 show a paramagnetic component Fe_{par} of the isomer shift typical for trivalent Fe. This component has been observed above T_p for most R variants, and it was thought to be related to the vicinity of Néel temperature. In $NdBaFe_2O_5$, however, the paramagnetic component is seen even below T_V, hence its origin remains unclear.

3.8. Effect of oxygen nonstoichiometry on charge ordering

Judging from $^{CN5}Fe^{2+}_{20T,CO}$, the concentration of charge-ordered iron states in $NdBaFe_2O_5$ is lower than in the Sm–Ho variants, Fig. 10. At $w=0$, it is 80% when estimated as the double of the amount of $^{CN5}Fe^{2+}_{20T,CO}$. This value includes both short- and long-range ordering as discussed in Ref. [6]. The concentration of charge-ordered species decreases linearly with nonstoichiometry increasing up to $w \approx 0.06$, after which a drop occurs. It was shown previously [22] that the concentrations of the valence-mixed Fe and the charge-ordered Fe follow different w dependencies. The lack of similar drop in the valence-mixed data simply means that the oxygen nonstoichiometry in $NdBaFe_2O_{5+w}$ is more detrimental to charge ordering than to valence mixing. It implies that a portion of charge-ordering defects chooses to participate in valence mixing above T_V.

The Mössbauer components belonging to defects in charge ordering (Fig. 12) differ somewhat from the defects in the valence mixing described in Section 3.7. This is not surprising because the cooperative forces to order orbitals (charges) are different from those to mix Fe^{2+} and Fe^{3+} into $Fe^{2.5+}$, and so would be the reasons for the respective failures to do so [22]. Thus the pentacoordinated trivalent twins (Section 3.7) are no longer present below T_V, and a single $^{CN5}Fe^{3+}_{50T}$ suffices. For the divalent defects the opposite is true; while one component was fitting the $NdBaFe_2O_5$ spectrum above T_p, two, $^{CN5}Fe^{2+}_{25T}$ and $^{CN5}Fe^{2+}_{30T}$, are needed below T_V.

4. Conclusions

Modeling Mössbauer electric-field gradients for $NdBaFe_2O_5$ and $GdBaFe_2O_5$ with structural parameters obtained from synchrotron X-ray diffraction of the same samples shows that Mössbauer spectrum "sees" the charge of the ordered orbitals of divalent iron below the Verwey transition; it registers the EFG of the ordered orbital. This is a direct proof of the orbital ordering, a feature that was inferred earlier [7] from structural distortions.

Similarly, the charge of the valence-mixing electron is detected. This proves that valence mixing in $RBaFe_2O_5$ proceeds between two Fe atoms and does not lead to any extensive delocalization, verifying conjectures based on elastic [4] and inelastic [23] neutron scattering and electrical conductivity [24] studies. The $RBaFe_2O_5$ Mössbauer measurement was for the first time taken above the Néel temperature, and the parameters of the $Fe^{2.5+}$ Mössbauer component were found unchanged. This finding confirms that the long-range magnetic order is irrelevant to valence mixing.

The choice of the structurally anomalous $NdBaFe_2O_5$ member of the Nd–Ho series improves our understanding of how sterical factors control charge ordering and valence mixing. The differences between $NdBaFe_2O_5$ and the Sm–Ho variants are consistent with the large Nd being detrimental to both processes.

The charge ordering is affected via the symmetry lowering adopted by charge-ordered $NdBaFe_2O_5$, as the tilt of the iron coordination square pyramids is less suited to accommodate the d_{xz} symmetry of the Fe^{2+} orbitals being ordered. The consequent decrease in orbital ordering in $NdBaFe_2O_5$ is manifested in both the internal field and the EFG at the Fe^{2+} Mössbauer nucleus: The ordered d_{xz} orbitals in $NdBaFe_2O_5$ produce only 60% of the orbit contribution to the field that would be generated by the
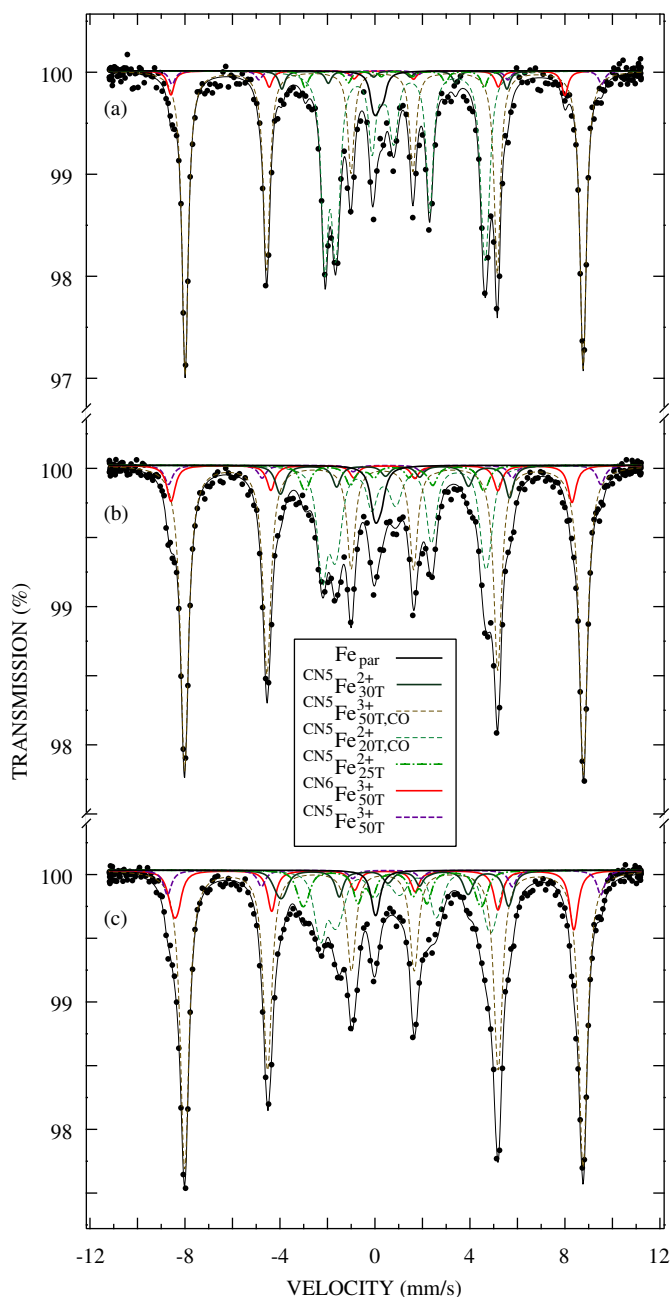
Fig. 12. Mössbauer spectra of NdBaFe$_2$O$_{5+w}$ at 77 K: (a) $w=0.001$, (b) $w=0.056$, and (c) $w=0.086$. Components used in the fitting are identified in the legend.

symmetric Sm–Ho variants. The same percentage is estimated from the orbital-charge (valence) contributions to EFG. When looked upon from the isomer-shift and intensity values, this same percentage follows, subdivided into the valence separation, which is ~80% of that for the GdBaFe$_2$O$_5$ (Section 3.4), and the concentration of the charge-ordered iron species, which is ~80% of those observed for $R =$ Eu and Sm [6] from Mössbauer

intensities. This gives a surprising conclusion that both the amount and the separation of the ordered charges are lower for NdBaFe$_2$O$_5$ than for its Sm–Ho variants, not just the one or the other. The valences assigned to the charge-ordered Mössbauer components therefore are not integer, but fractional, of decimal precision. This might be valid even if Mössbauer parameters at favorable conditions suggest charge ordering close to integer valences, as it is so in powder samples of EuBaFe$_2$O$_5$ [6] or in single crystalline Fe$_2$OBO$_3$ [25].

The valence mixing is affected directly by the size of the Nd atom that further separates the structural layers of Fe atoms facing each other. As a consequence, NdBaFe$_2$O$_5$ has only 84% of the Fe$^{2.5+}$ concentration found [6] in EuBaFe$_2$O$_5$.

Acknowledgments

References

[1] M.B. Robin, P. Day, Adv. Inorg. Chem. Radiochem. 10 (1967) 247–422.
[2] P. Karen, P.M. Woodward, J. Lindén, T. Vogt, A. Studer, P. Fisher, Phys. Rev. B 64 (2001) 214405/1–14.
[3] P. Karen, P.M. Woodward, P.N. Santosh, T. Vogt, P.W. Stephens, S. Pagola, J. Solid State Chem. 167 (2002) 480–493.
[4] P.M. Woodward, E. Suard, P. Karen, J. Am. Chem. Soc. 125 (2003) 8889–8899.
[5] P. Karen, J. Solid State Chem. 177 (2004) 281–292.
[6] P. Karen, K. Gustafsson, J. Lindén, J. Solid State Chem. 180 (2007) 138–147.
[7] P.M. Woodward, P. Karen, Inorg. Chem. 42 (2003) 1121–1129.
[8] J. Lindén, P. Karen, A. Kjekshus, J. Miettinen, T. Pietari, M. Karppinen, Phys. Rev. B 60 (1999) 15251–15260.
[9] P. Karen, J. Solid State Chem. 179 (2006) 3167–3183.
[10] I.N. Sora, Q. Huang, J.W. Lynn, N. Rosov, P. Karen, A. Kjekshus, V.L. Karen, A.D. Mighell, A. Santoro, Phys. Rev. B 49 (1994) 3465–3472.
[11] A.C. Larson, R.B. Von Dreele, General Structure Analysis System (GSAS), Los Alamos National Laboratory Report LAUR 86-748, 2000.
[12] P.W. Stephens, J. Appl. Cryst. 32 (1999) 281–289.
[13] P. Karen, J. Solid State Chem. 170 (2003) 9–23.
[14] J. Ren, W. Liang, M.H. Whangbo, Crystal and Electronic Structure Analysis Using CAESAR, PrimeColor Software Inc., Cary, NC, 1998.
[15] R. Gütlich, in: U. Gonser (Ed.), Topics in Applied Physics V, Mössbauer Spectroscopy I, Springer, Berlin1975, p. 61.
[16] Z. Su, P. Coppens, Acta Crystallogr. Sec. A 52 (1996) 748–756.
[17] G. Martínez-Pinedo, P. Schwerdtfeger, E. Caurier, K. Langanke, W. Nazarewicz, T. Söhnel, Phys. Rev. Lett. 87 (2001) 062701/1–4.
[18] I.D. Brown, The Chemical Bond in Inorganic Chemistry, The Bond Valence Model, Oxford University Press, 2002, pp. 225–226.
[19] J. Lindén, P. Karen, H. Yamauchi, M. Karppinen, Hyperfine Interactions 156–157 (2004) 321–325.
[20] C. Spiel, P. Blaha, K. Schwarz, Phys. Rev. B 79 (2009) 115123-1–115123-13.
[21] P. Karen, K. Gustafsson, J. Lindén, J. Solid State Chem. 180 (2007) 2641–2642.
[22] P. Karen, K. Gustafsson, J. Lindén, J. Solid State Chem. 180 (2007) 148–157.
[23] S. Chang, P. Karen, M.P. Hehlen, F.R. Trouw, R.J. McQueeney, Phys. Rev. Lett. 99 (2007) 037202/1–4.
[24] J. Lindén, P. Karen, J. Nakamura, M. Karppinen, H. Yamauchi, Phys. Rev. B 73 (2006) 064415/1–7.
[25] M. Angst, R.P. Hermann, W. Schweika, J.-W. Kim, P. Khalifah, H.J. Xiang, M.-H. Whangbo, D.-H. Kim, B.C. Sales, D. Mandrus, Phys. Rev. Lett. 99 (2007) 256402/1–4.